Why did deep convection persist over four consecutive winters (2015-2018) Southeast of Cape Farewell?

Patricia ZUNINO[1], Herlé MERCIER[2] and Virginie THIERRY[3].

1 Altran Technologies, Technopôle Brest Iroise, Site du Vernis, 300 rue Pierre Rivoalon, 29200 Brest, France

2 CNRS, University of Brest, IRD, Ifremer, Laboratoire d'Océanographie Physique et Spatiale (LOPS), IUEM, ZI de la pointe du diable, CS 10070 - 29280 Plouzané, France

3 Ifremer, University of Brest, CNRS, IRD, Laboratoire d'Océanographie Physique et Spatiale (LOPS), IUEM, ZI de la pointe du diable, CS 10070 - 29280 Plouzané, France

Corresponding author: patricia.zuninorodriguez@altran.com

ABSTRACT

After more than a decade of shallow convection, deep convection returned to the Irminger Sea in 2008 and occurred several times since then to reach exceptional convection depths (>1,500 m) in 2015 and 2016. Additionally, deep mixed layers larger than 1,600 m were also reported Southeast of Cape Farewell in 2015. In this context, we used Argo data to show that deep convection occurred Southeast of Cape Farewell (SECF) in 2016 and persisted during two additional years in 2017 and 2018 with maximum convection depth larger than 1,300 m. In this article, we investigate the respective roles of air-sea buoyancy flux and preconditioning of the water column (ocean interior buoyancy content) to explain this 4-year persistence of deep convection SECF. We analyzed the respective contributions of the heat and freshwater components. Contrary to the very negative air-sea buoyancy flux that was observed during winter 2015, the buoyancy fluxes over the SECF region during winters 2016, 2017 and 2018 were close to the climatological average. We estimated the preconditioning of the water column as the buoyancy that needs to be removed (B) from the end of summer water column to homogenize it down to a given depth. B was lower for winters 2016 – 2018 than for the 2008 – 2015 winter mean, due especially to a vanishing stratification from 600 m down to ~1,300 m. It means that less air-sea buoyancy loss was necessary to reach a given convection depth than in the mean and once convection reached 600 m little additional buoyancy loss was needed to homogenize the water column down to 1,300 m. We showed that the decrease in B was due to the combined effects of the local cooling of the intermediate water (200 – 800 m) and the advection of a negative S anomaly in the 1,200 – 1,400 m layer. This favorable preconditioning permitted the very deep convection observed in 2016 – 2018 despite the atmospheric forcing was close to the climatological average.

2

1. INTRODUCTION

Deep convection is the result of a process by which surface waters loose buoyancy due to atmospheric forcing and sink into the interior of the ocean. It occurs only where specific conditions are met including large air-sea buoyancy loss and favorable preconditioning (i.e. low stratification of the water column) (Marshall & Schott, 1999). In the Subpolar North Atlantic (SPNA), deep convection takes place in the Labrador Sea, South of Cape Farewell and in the Irminger Sea (Kieke & Yashayaev, 2015; Pickart et al., 2003; Piron et al., 2017). Deep convection connects the upper and lower limbs of the Meridional Overturning Circulation (MOC) and transfers climate change signals from the surface to the ocean interior.

Observing deep convection is difficult because it happens on short time and small spatial scales and during periods of severe weather conditions (Marshall & Schott, 1999). The onset of the Argo program at the beginning of the 2000s has considerably increased the number of available oceanographic data throughout the year. Although the sampling characteristics of Argo are not adequate to observe the small scales associated with the convection process itself, Argo data allow the description of the overall intensity of the event and the characterization of the properties of the water masses formed in the winter mixed layer as well (e.g., Yashayaev and Loder, 2017).

In the Labrador Sea, deep convection occurs every year, yet with different intensity (e.g., Yashayaev and Clarke, 2008; Kieke and Yashayaev, 2015). In the Irminger Sea, Argo and mooring data showed that convection deeper than 700 m happened during winters 2008, 2009, 2012, 2015 and 2016 (Väge et al., 2009; de Jong et al., 2012; Piron et al., 2015; de Jong & de Steur, 2016; Fröb et al., 2016; Piron et al., 2017; de Jong et al., 2018). Moreover, in winter 2015, deep convection was also observed south of Cape Farewell (Piron et al., 2017). Excluding winter 2009 when the deep convection event was made possible thanks to a favorable preconditioning (de Jong et al., 2012), all events coincided with strong atmospheric forcing (air-sea heat loss). Prior to 2008, only few deep convection events were reported because the mechanisms leading to it were not favorable (Centurioni and Gould, 2004) or because the observing system was not adequate (Bacon, 1997; Pickart et al., 2003). Nevertheless, the hydrographic properties from the 1990s suggested that deep convection reached as deep as 1,500 m in the Irminger Sea during winters 1994 and 1995 (Pickart et al., 2003), and as deep as 1,000 m south of Cape Farewell during winter 1997 (Bacon et al., 2003).

The convection depths that were reached in the Irminger Sea and south of Cape Farewell at the end of winter 2015 were the deepest observed in these regions since the beginning of the 21st century (de Jong et al., 2016; Piron et al., 2017, Fröb et al., 2016). In this work, we show that deep convection

3

103   also happened in a region between south of Cape Farewell and the Irminger Sea (the pink box in

104   Figure 1) every winter from 2016 to 2018. Hereinafter, we will refer to this region as Southeast Cape

105   Farewell (SECF). We investigated the respective role of atmospheric forcing (air-sea buoyancy flux)

106   and preconditioning (ocean interior buoyancy content) in setting the convection intensity. We also

107   disentangled the relative contribution of salinity and temperature anomalies to the preconditioning.

108   The paper is organized as follow. The data are described in Sect. 2. The methodology is explained in

109   Sect. 3. We expose our results in Sect. 4 and discuss them in Sect. 5. Conclusions are listed in Sect. 6.

110

2. DATA

112   We used temperature (T), salinity (S) and pressure (P) data measured by Argo floats north of 55°N in

113   the Atlantic Ocean. These data were collected by the International Argo program

114   (http://www.argo.ucsd.edu/), http://www.jcommops.org/) and downloaded from the Coriolis Data

115   Center (http://www.coriolis.eu.org/). Only data flagged as good (quality Control < 3, Argo Data

116   Management Team, 2017) were considered in our analysis. Potential temperature (θ), density (ρ)

117   and potential density anomaly referenced to the surface and 1000 dbar (σ_0 and σ_1, respectively) were

118   estimated from T, S and P data using TEOS-10 (http://www.teos-10.org/).

119   We used two different gridded products of ocean T and S: ISAS and EN4. ISAS (Gaillard et al., 2016;

120   Kolodziejczyk et al., 2017) is produced by optimal interpolation of *in situ* data. It provides monthly

121   fields, at 152 depth levels, at 0.5° resolution, from 2002 to 2015. Near real time data are also

122   availaible for 2016 and 2018. EN4 (Good et al., 2013) is an optimal interpolation of *in situ* data; it

123   provides monthly T and S at 1° spatial resolution and at 42 depth levels, for the period 1900 to

124   present.

125   Net air-sea heat flux (Q , the sum of radiative and turbulent fluxes), evaporation (E), precipitation (P),

126   wind stress (τ_x and τ_y) and sea surface temperature (SST) data were obtained from ERA-Interim

127   reanalysis (Dee et al., 2011). ERA-Interim provides data with a time resolution of 12h and a spatial

128   resolution of 0.75°, respectively. The air-sea freshwater flux (FWF) was estimated as E - P.

129   We used monthly Absolute Dynamic Topographic (ADT), which was computed from the daily 0.25° -

130   resolution ADT data provided by CMEMS (Copernicus Marine and Environment Monitoring Service,

131   http://www.marine.copernicus.eu).

132

3. METHODS

4

3.1 Quantification of the deep convection

We characterized the convection in the SPNA in winters 2015-2018 by estimating the mixed layer depths (MLD) for all Argo profiles collected in the SPNA north of 55°N from 1st January to 30th April of each year (Fig. 1). The MLD was estimated as the shallowest of the three MLD estimates obtained by applying the threshold method (de Boyer Montégut et al., 2004) to θ, S and ρ profiles separately. The threshold method computes the MLD as the depth at which the difference between the surface (30 m) and deeper levels in a given property is equal to a given threshold. In case visual inspection of the winter profiles showed a thin stratified layer at the surface, a slightly deeper level (< 150 m) was considered as surface reference level. Following Piron et al. (2017), this threshold was taken equal to 0.01 kg m^{-3} for ρ. For θ and S, we selected thresholds of 0.1°C and 0.012 respectively because they correspond to the threshold of 0.01 kg m^{-3} in ρ. The latter was previously shown to perform well in the subpolar gyre on density profiles (Piron et al., 2016). The criteria on temperature and salinity were chosen to perform well when temperature and salinity anomalies within the density-defined mixed layer are density compensated. Our MLD estimates are comparable to those obtained using MLD determination based on Pickart et al. (2002)'s methods (see section S1, Fig. S1 and Fig. S2 in supplementary material).

In this paper, deep convection is characterized by profiles with MLD deeper than 700m (colored points in Fig. 1) because it is the minimum depth that should be reached for renewing Labrador Sea Water (LSW) (Yashayaev et al., 2007; Piron et al., 2016). The winter MLD and the associated θ, S and ρ properties were examined for the Labrador Sea and the SECF region by considering the profiles inside the cyan and pink boxes in Fig. 1, respectively. Those two boxes were defined to include all Argo profiles with MLD deeper than 700 m during 2016 – 2018 and the minimum of the monthly ADT for either the SECF region or the Labrador Sea. No deep MLD was recorded in the northernmost part of the Irminger Sea during this period. We computed the maximum MLD and the MLD third quartile (Q$_3$) from profiles with MLD greater than 700m in each of the two boxes separately. Q$_3$ is the MLD value that is exceeded by 25% of the profiles and is equivalent to the aggregate maximum depth of convection defined by Yashayaev and Loder (2016). Hereafter, we refer to Q$_3$ as the aggregate maximum depth of convection. The properties (ρ, θ and S) of the mixed layers were defined for each winter as the vertical mean from 200 m to the MLD of all profiles with MLD deeper than 700 m. For further use, we define the deep convection period as follows. For a given winter, the deep convection period begins the day when the first profile with a deep (> 700m) mixed layer is detected and ends the day of the last detection of a deep mixed layer.

5

3.2. Time series of atmospheric forcing

The air-sea buoyancy flux (B_{surf}) was calculated as the sum of the contributions of Q and FWF (Gill, 1982; Billheimer & Talley, 2013). It reads:

$$B_{surf} = \frac{\alpha g}{\rho_0 c_p} Q - \beta g \, SSS \, FWF \qquad \text{Eq. (1)}$$

Where α and β are the coefficients of thermal and saline expansions, respectively, estimated from surface T and S. The gravitational acceleration g is equal to 9.8 m s^{-2}, the reference density of sea water ρ_0 is equal to 1026 kg m^{-3} and heat capacity of sea water C_p is equal to 3990 J kg $^{-1}$ °C^{-1}. SSS is the sea surface salinity. Q and FWF are in W m^{-2} and m s^{-1}, respectively.

For easy comparison with previous results, which only considered the heat component of the buoyancy air-sea flux (e.g. Yashayaev & Loder, 2017; Piron et al., 2017; Rhein et al., 2017), B_{surf}, in m^2 s^{-3}, was converted to W m^{-2} following Eq. (2) and noted B_{surf}^*

$$B_{surf}^* = \frac{\rho_0 \, c_p}{g \, \alpha} B_{surf} \qquad \text{Eq. (2)}$$

The FWF was also converted to W m^{-2} using:

$$\text{FWF}^* = \text{FWF} \; \beta \; SSS \; \frac{\rho_0 \, c_p}{\alpha} \qquad \text{Eq. (3)}$$

We also computed the horizontal Ekman buoyancy flux (BF_{ek}), which can be decomposed into the horizontal Ekman heat flux (HF_{ek}) and salt flux (SF_{ek}). Noting:

$$BF_{ek} = -g \, (U_e \partial_x SSD + V_e \partial_y SSD) \frac{C_p}{\alpha . g} \qquad \text{Eq. (4)}$$

$$HF_{ek} = -(U_e \partial_x SST + V_e \partial_y SST) \, \rho_0 \, C_p \qquad \text{Eq. (5)}$$

$$SF_{ek} = -(U_e \partial_x SSS + V_e \partial_y SSS) \frac{\beta \, \rho_0 \, C_p}{\alpha} \qquad \text{Eq. (6)}$$

$BF_{ek} = SF_{ek} - HF_{ek}$. U_e and V_e are the eastward and northward components of the Ekman horizontal transport estimated from the wind stress meridional and zonal components. SSD, SST and SSS are ρ, T and S at the surface of the ocean. BF_{ek}, HF_{ek} and SF_e are in J s^{-1} m^{-2}. Because ERA-Interim does not supply SSD or SSS, they were estimated from EN4 as follows. The monthly T and S data at 5 m depth from EN4 were interpolated on the same time and space grid as the air-sea fluxes from ERA-Interim (12h and 0.75°, respectively). SSD was estimated from those interpolated EN4 data (SST and SSS). Properties at 5 m depth were considered to be representative of the Ekman layer. Data at locations

193 where ocean bottom was shallower than 1000 m were excluded from the analysis to avoid regions
194 covered by sea-ice.

195 Following Piron et al. (2016), the time series of atmospheric forcing were estimated for the SECF
196 region and the Labrador Sea as follows. First, the gridded air-sea flux data and the horizontal Ekman
197 fluxes were averaged over the pink (SECF region) and cyan (Labrador Sea) boxes (Fig. 1). Second, we
198 estimated the accumulated fluxes from 1 September to 31 August the year after. Finally, we
199 computed the time series of the anomalies of the accumulated fluxes from 1 September to 31 August
200 with respect to the 1993 – 2016 mean.

201 Finally, in order to quantify the net intensity of the atmospheric forcing over the winter, we
202 computed estimates of B_{surf}* + BF_{ek} fluxes accumulated from 1 September to 31 March the year after.
203 Following Piron et al. (2017), the associated errors were calculated by a Monte Carlo simulation using
204 50 random perturbations of Q, FWF and B_{surf}. The error amounted to 0.05, 0.04 and 0.03 J m^{-2} for
205 B_{surf}*, Q and FWF*, respectively. The error of the horizontal Ekman buoyancy transport was also
206 estimated by a Monte Carlo simulation and amounted to 0.04 J m^{-2}.

207 3.3. Preconditioning of the water column

208 The preconditioning of the water column was evaluated as the buoyancy that has to be removed
209 $(B(zi))$ from the late summer density profile to homogenize it down to a depth zi. It reads:

210 $B(zi) = \frac{g}{\rho_0} \sigma_0(zi)zi - \frac{g}{\rho_0} \int_{z_i}^{o} \sigma_0 (z)dz$ Eq. (7)

211 $\sigma_0(z)$ is the vertical profile of potential density anomaly estimated from the profiles of T and S
212 measured by Argo floats in September in the given region (pink or cyan box in Fig. 1).

213 Following Schmidt and Send (2007), we split B into a temperature (B_θ) and salinity (B_S) term:

214 $B_\theta(zi) = -(g \alpha \theta(zi) zi - g \alpha \int_{zi}^{o} \theta(z) dz)$ Eq. (8)

215 $B_S(zi) = g \beta S(zi) zi - g \beta \int_{zi}^{o} S (z)dz$ Eq. (9)

216 In order to compare the preconditioning with the heat to be removed and/or air-sea heat fluxes, B,
217 B_θ and B_S are reported in J m^{-2}. B, B_θ and B_S were estimated for a given year from the mean of all
218 September profiles of B, B_θ and B_S. The associated errors were estimated as std(B)/√n, where n is
219 the number of profiles used to compute the September mean values.
220

4. RESULTS

4.1. Intensity of deep convection and properties of newly formed LSW

We examine the time-evolution of the winter mixed layer SECF since the exceptional convection event of winter 2015 (W2015 hereinafter) (Table 1 and Figs. 1 - 3). In W2015, we recorded a maximum MLD of 1,710 m south of Cape Farewell (Fig. 1a), in line with Piron et al. (2017). The maximum MLD of 1,575 m observed for W2016 (Fig. 1b) is compatible with the active mixed layer > 1,500 m observed in a mooring array in the central Irminger Sea by de Jong et al. (2018). For W2015 and W2016, the aggregate maximum depth of convection was 1,205 m and 1,471 m, respectively (Table 1). In W2017, deep convection was observed from three Argo profiles (Fig. 1c and Fig. 2a-c). The maximum MLD of 1,400 m was observed on 16th March 2017 at 56.65°N – 42.30°W. In W2018, the maximum MLD of 1,300 m was observed on 24 February at 58.12°N, 41.84°W (Fig. 1d, 2d-f). Float 5903102 measured MLD of 1,100 m South of Cape Farewell (Fig. 1d), but the estimated MLDs coincided with the deepest levels of measurement of the float so that these estimates, possibly biased low (see Fig. 2d-f), were discarded from our analysis. These results show that convection deeper than 1,300 m occurred during four consecutive winters SECF.

Although the number of floats showing deep convection in W2017 and W2018 was small (3 and 2 floats), it represented a significant percentage of the floats operating in the SECF box at that time. The percentage of floats showing deep convection in the SECF region was computed for the deep convection periods defined from 15 January 2015 to 21 April 2015, 22 February 2016 to 21 March 2016, 16 March 2017 to 4 April 2017 and 24 February 2018 to 26 March 2018. The longest period of deep convection occurred in W2015, the shortest in 2017. The percentage of floats showing deep convection during the deep convection period are 73%, 50%, 33 % and 50%, for winters 2015, 2016, 2017 and 2018, respectively. The lowest % is found for W2017, but it is still substantial. It might reflect that for this specific year floats showing deep MLD were found in the southwestern corner of the SECF box only, suggesting that convection did not occur over the full box.

The properties (σ_0, S and θ) of the end of winter mixed layer were estimated for the four winters (Table 1 and Fig. 3). We observed that, between W2015 and W2018, the water mass formed by deep convection significantly densified and cooled by 0.019 kg m^{-3} and 0.215°C, respectively (see Table 1 and Fig. 3).

In the Labrador Sea, the aggregate maximum depth of convection increased from 2015 to 2018 (see Table 1). Deep convection observed in the Labrador Sea in W2018 was the most intense since the beginning of the Argo era (see Fig. 2c in Yashayaev & Loder, 2016). From W2015 to W2018, newly

8

253   formed LSW cooled, became saltier and densified by 0.134°C, 0.013 and 0.023 kg m^{-3}, respectively

254   (Table 1).

255   The water mass formed SECF is warmer and saltier than that formed in the Labrador Sea (Fig. 3). The

256   deep convection SECF is always shallower than in the Labrador Sea. This result is discussed later in

257   Sect. 5.

4.2. Analysis of the atmospheric forcing Southeast of Cape Farewell

259   The seasonal cycles of B_{surf}* and Q are in phase and of the same order of magnitude, while FWF*,

260   which is positive and one order of magnitude lower than Q, does not present a seasonal cycle (Fig.

261   S3). The means (1993 – 2018) of the cumulative sums from 1 September to 31 March of Q, FWF* and

262   B_{surf}* estimated over the SECF box (Fig. 1) are - 2.46 ± 0.43 x 10^9 J m^{-2}, 0.28 ± 0.10 x 10^9 J m^{-2} and -

263   2.22 ± 0.49 x 10^9 J m^{-2}, respectively. B_{surf}* is 10 % lower on average than Q because of the buoyancy

264   addition by FWF*. Considering the Ekman transports, the 1993 – 2018 means of the accumulated

265   BF_{ek}, HF_{ek} and SF_{ek} from 1 September to 31 March amount to 0.37 ± 1.15 x 10^8 J m^{-2}, - 0.35 ± 1.36 x

266   10^8 J m^{-2}, and 0.02 ± 2.04 x 10^8 x 10^9 J m^{-2}, respectively. The horizontal Ekman heat flux is negative,

267   while the Ekman buoyancy flux is positive. This buoyancy gain indicates a southeastward transport of

268   surface freshwater caused by dominant winds from the southwest. Noteworthy, BF_{ek} is one order of

269   magnitude smaller than the B_{surf}*.

270   The total atmospheric forcing SECF was quantified as the sum of B_{surf}* and BF_{ek}. The anomalies of

271   accumulated fluxes from 1 September to 31 August the year after, with respect to the mean 1993 –

272   2016, are displayed in Fig. 4 for the SECF box. The grey line in Fig. 4a is the total atmospheric forcing

273   anomaly (B_{surf}* plus BF_{ek}). We identify years with very negative buoyancy loss in the SECF region, e.g.

274   1994, 1999, 2008, 2012 and 2015. The very negative anomalies of atmospheric forcing in 1999 and

275   2015 were caused by the very negative anomalies in both B_{surf}* (Fig. 4a) and BF_{ek} (Fig.4d). This

276   correlation was not observed for all the years presenting a negative anomaly of atmospheric forcing.

277   Noteworthy, during W2016, W2017 and W2018, the anomaly of atmospheric forcing was close to

278   zero.

279   Contrary to the very negative anomaly in atmospheric fluxes over the SECF region observed for

280   W2015, the atmospheric fluxes were close to the mean during W2016, W2017 and W2018.

4.3. Analysis of the preconditioning of the water column Southeast of Cape

Farewell

9

283   Our hypothesis is that the exceptional deep convection that happened in W2015 in the SECF region

284   favorably preconditioned the water column for deep convection the following winters. The time-

285   evolutions of θ, S, σ_1 and of $\Delta\sigma_1$=0.01 kg m^{-3} layer thicknesses (Fig. 5) show a marked change in the

286   hydrographic properties of the SECF region at the beginning of 2015 caused by the exceptional deep

287   convection that occurred during W2015 (see Piron et al., 2017). The intermediate waters (500 –

288   1,000 m) became colder than the years before and, despite a slight decrease in salinity, the cooling

289   caused the density to increase (Fig. 5c). Fig. 5d shows $\Delta\sigma_1$=0.01 kg m^{-3} layer thicknesses larger than

290   600 m appearing at the end of W2015 for the first time since 2002. In the density range 32.36 – 32.39

291   kg m^{-3}, these layers remained thicker than ~450 m during W2016 to W2018. This indicates low

292   stratification at intermediate depths and a favorable preconditioning of intermediate waters for deep

293   convection initiated by W2015 deep convection. The denser density of the core of the thick layers in

294   2017 -2018 compared with 2015 - 2016 agrees with the densification of the mixed layer SECF shown

295   in Table 1 and Fig. 3.

296   B(zi) is our estimate of the preconditioning of the water column before winter (see Method). Fig. 6a

297   shows that, deeper than 100 m, B for W2016, W2017 and W2018 was smaller than B for W2015 or B

298   for the mean W2008 – W2014. Furthermore, for W2016, W2017 and 2018, B remained nearly

299   constant with depth between 600 and 1,300 m, which means that once the water column has been

300   homogenized down to 600 m, little additional buoyancy loss results in the homogenization of the

301   water column down to 1,300 m. Both conditions (i) less buoyancy to be removed and (ii) absence of

302   gradient in the B profile down to 1,300 m indicate a more favorable preconditioning of the water

303   column for W2016, W2017 and W2018 than during W2008 – W2015.

304   To understand the relative contributions of θ and S to the preconditioning, we computed the thermal

305   (B_θ) and haline (B_S) components of B (B = B_θ + B_S). In general, B_θ (B_S) increases with depth when θ

306   decreases (S increases) with depth. On the contrary, a negative slope in a B_θ (B_S) profile corresponds

307   to θ increasing (S decreasing) with depth and is indicative of a destabilizing effect. The negative

308   slopes in B_θ and B_s profiles are not observed simultaneously because density profiles are stable.

309   We describe the relative contributions of B_θ and B_s to B by looking first at the mean 2008 – 2014

310   profiles (discontinuous blue lines in Fig. 6). B_θ accounts for most of the increase in B from the surface

311   to 800 m and below 1,400 m (see Fig. 6a and Fig. 6b). The negative slope in the B_s profile between

312   800 – 1,000 m (Fig. 6c) slightly reduces B (Fig. 6a) and is due to the decrease in S associated with the

313   core of LSW (see Fig. 3 in Piron et al., 2016). In the layer 1,000 – 1,400 m, the increase in B (Fig. 6a) is

314   mainly explained by the increase in B_s (Fig. 6c), which follows the increase in S in the transition from

315   LSW to Iceland Scotland Overflow Water (ISOW). This transition layer will be referred to hereinafter

10

316   as the deep halocline. The evaluation of the preconditioning of the water column was usually

317   analyzed in terms of heat (e.g., Piron et al., 2015; 2017). The decomposition of B in B_θ and B_s reveals

318   that θ governs B in the layer 0 – 800 m. S tends to reduce the stabilizing effect of θ in the layer 800 –

319   1,000 m, and reinforces it in the layer 1,000 – 1,400 m by adding up to 1×10^9 J m^2 to B.

320   In order to further understand why the SEFC region was favorably preconditioned during winters

321   2016 – 2018, we compare the B_θ and B_s of W2017, which was the most favorably preconditioned

322   winter, with the mean 2008 – 2014 (Fig. 7a). From the surface to 1,600 m, B_θ and B_s were smaller for

323   W2017 than for the mean 2008 – 2014. There are two additional remarkable features. First, in the

324   layer 500 – 1000 m, the large reduction of B_θ compared to the 2008 – 2014 mean, mostly explains

325   the decrease in B in this layer. Second, the more negative value of B_s in the layer 1,100 – 1,300 m,

326   compared to the 2008 – 2014 mean, eroded the B_θ slope, making the B profile more vertical for

327   W2017 than for the mean. The more negative contribution of B_s in the layer 1,100 – 1,300 m comes

328   from the fact that the deep halocline was deeper for W2017 (1,300 m, see orange dashed line in Fig.

329   7a) than for the mean 2008 – 2014 (1,000 m, see blue dashed line in Fig. 7a). Finally, we note that the

330   profiles of $B(z_i)$, $B_\theta(z_i)$ and $B_s(z_i)$ for W2016 and W2018 are more similar to the profiles of W2017 than

331   to those of W2015 or to the mean 2008 – 2014 (see Fig. 6), which indicates that the water column

332   was also favorably preconditioned for deep convection in W2016 and W2018 for the same reasons as

333   in W2017.

334   The origin of the changes in B is now discussed from the time evolutions of the monthly anomalies of

335   θ, S and σ_0 at 58°N – 40°W that is at the center of the SECF box (Fig. 8). The time evolutions there are

336   similar to those at any other location inside the SECF box. These anomalies were computed using

337   ISAS (Gaillard et al., 2016) and were referenced to the monthly mean of 2002 – 2016. A positive

338   anomaly of σ_0 appeared in 2014 between the surface and 600 m (Fig. 8a) and reached 1,200m in

339   2015 and beyond. This positive anomaly of σ_0 correlates with a negative anomaly of θ. The latter,

340   however, reached ~1,400 m depth in 2016 that is deeper than the positive anomaly of σ_0. The

341   negative anomaly of S between 1,000 - 1,500 m that appeared in 2015 and strongly reinforced in

342   2016 caused the negative anomaly in σ_0 between 1,200 – 1,500 m (the density anomaly caused by

343   the negative anomaly in θ between 1,200 – 1,400 m does not balance the density anomaly caused by

344   the negative anomaly of S).

345   The θ and S anomalies in the water column during 2016 – 2018 explain the anomalies of B, B_θ and B_s

346   and can be summarized as follows. On the one hand, the properties of the surface waters (down to

347   500 m) were colder than previous years and, despite they were also fresher, they were denser. The

348   density increase in the surface water reduced the density difference with the deeper-lying waters.

11

349 The intermediate layer (500 – 1,000 m) was also favorably preconditioned due to the observed

350 cooling. Additionally, in the layer 1,100 – 1,300 m, the large negative anomaly of B_s with respect to its

351 mean is explained by the decrease in S in this layer, which caused a decrease in σ_0 and, consequently,

352 reduced the σ_0 difference with the shallower-lying water. The decrease in S also resulted in a

353 deepening of the deep halocline.

4.4. Atmospheric forcing versus preconditioning of the water column

355 We now use the estimates of the accumulated atmospheric forcing (B_{surf}* + BF_{ek}) from 1 September

356 to 31 March the year after (see Fig. S4) to predict the maximum convection depth for a given winter

357 based on September profiles of B. The predicted convection depth is determined as the depth at

358 which $B(z_i)$ (Fig. 6a) equals the accumulated atmospheric forcing. The associated error was estimated

359 by propagating the error in the atmospheric forcing (0.05×10^9 J m^{-2}). The accumulated atmospheric

360 forcing amounted to $-3.21 \times 10^9 \pm 0.05$ J m^{-2}, $-2.21 \pm 0.04 \times 10^9$ J m^{-2}, $-2.01 \pm 0.05 \times 10^9$ J m^{-2} and -2.47

361 $\pm 0.05 \times 10^9$ J m^{-2} for W2015, W2016, W2017 and W2018, respectively. We found predicted

362 convection depths of $1,085 \pm 20$ m, $1,285 \pm 20$ m, $1,415 \pm 20$ m and $1,345 \pm 20$ m for W2015, W2016,

363 W2017 and W2018, respectively. We consider the aggregate maximum depth of convection as the

364 observed estimate of the MLD (Table 1). The predicted MLD agrees with the observed MLD within ±

365 200 m. The differences could be due to errors in the atmospheric forcing (Josey et al., 2018), lateral

366 advection and/or spatial variation in the convection intensity within the box not captured by the

367 Argo sampling.

368 The satisfactory predictability of the convection depth with our 1-D model indicates that deep

369 convection occurred locally. In spite the atmospheric forcing was close to mean (1993 – 2016)

370 conditions during W2016, W2017 and W2018, convection depths > 1,300 m were reached in the

371 SECF region. This was only possible thanks to the favorable preconditioning.

372

5. DISCUSSION

374 Deep convection happens in the Irminger Sea and South of Cape Farewell during specific winters

375 characterized by a strong atmospheric forcing (high buoyancy loss), a favorable preconditioning (low

376 stratification) or both at the same time (Bacon et al., 2003; Pickart et al., 2003). In the Irminger Sea,

377 strong atmospheric forcing explained for instance the very deep convection (reaching depth greater

378 than 1,500 m) observed in the early 90s (Pickart et al., 2003) and in W2015 (de Jong et al. 2016; Fröb

379 et al., 2016; Piron et al., 2017). It explained as well the return of deep convection in W2008 (Väge et

380 al., 2009) and in W2012 (Piron et al., 2016). The favorable preconditioning caused by the

381 densification of the mixed layer during W2008 favored a new deep convection event in W2009

12

382   despite neutral atmospheric forcing (de Jong et al., 2012). Similarly, the preconditioning observed

383   after W2015 in the SECF region favored deep convection in W2016 (this work). The favorable

384   preconditioning persisted three consecutive winters (2016 – 2018) in the SECF region, which allowed

385   deep convection although atmospheric forcing was close to the climatological values. Why did this

386   favorable preconditioning persist in time?

387   We previously showed that during 2016 – 2018 two hydrographic anomalies affected different

388   ranges of the water column in SECF box: a cooling intensified in the layer 200 – 800 m and a

389   freshening intensified in 1,000 – 1,500 m layer. Those resulted in a decrease in the vertical density

390   gradient between the intermediate and the deeper layers creating a favorable preconditioning of the

391   water column. Note that the cooling affected the layer from surface to 1,400 m and the freshening

392   affected the layer from near surface to 1,600 m, but the cooling and the freshening were intensified

393   at different depth ranges (Fig. 8).

394   We see in Fig. 5a a sudden decrease in θ in the intermediate layers in 2015 compared to the previous

395   years. It indicates that the decrease in θ of the intermediate layer likely originated locally during

396   W2015 when extraordinary deep convection happened. A slight freshening of the water column

397   (400- 1,500 m) appeared in 2015, likely caused by the W2015 convection event, then it decreased

398   before a second S anomaly intensified in 2016 between 1,100 and 1,400 m (Fig. 8c). It is unlikely that

399   this second anomaly was exclusively locally formed by deep convection because it intensified during

400   summer 2016. Our hypothesis is that this second S anomaly originated in the Labrador Sea and was

401   further transferred to the SECF region by the cyclonic circulation encompassing the Labrador Sea and

402   Irminger Sea at these depths (Daniault et al., 2016; Ollitrault & Colin de Verdière, 2014; Lavander et

403   al., 2000 ; Straneo et al., 2003). It is corroborated by the 2D evolution of the anomalies in S in the

404   layer 1,200 – 1,400 m (Fig. 9): a negative anomaly in S appeared in the Labrador Sea in February

405   2015, which was transferred southward and northeastward in February 2016 and intensified over the

406   whole SPNA in February 2017. By this mechanism, the advection from the Labrador Sea contributed

407   to create property anomalies in the water column. However, the buoyancy budget showed that this

408   was a minor contribution compared to the buoyancy loss due to the local air-sea flux, even if it was

409   essential to preconditioning the water column for deep convection.

410   We now compare the atmospheric forcing and the preconditioning of the water column in the SECF

411   region with those of the nearby Labrador Sea where deep convection happens almost every year.

412   The atmospheric forcing over the Labrador Sea is ~15 % larger than that over the SECF region: the

413   means (1993 - 2018) of the atmospheric forcing, defined as the time accumulated $B_{surf}^* + BF_{ek}$ from 1

414   September to 31 March the year after, are -2.61 ± 0.55 x 10^9 J m^{-2} in the Labrador Sea and -2.18 ±

13

0.54 x 10^9 J m^{-2} in the SECF region. The difference was larger during the period 2016 – 2018 when the atmospheric forcing equaled -3.10 ± 0.19 x 10^9 J m^{-2} in the Labrador Sea and -2.23 ± 0.23 x 10^9 J m^{-2} in the SECF region. In terms of preconditioning, the 2008 – 2014 mean B profile (blue continuous lines in Fig. 7) was lower by ~0.5 x 10^9 J m^{-2} in the Labrador Sea than SECF for the surface to 1,000 m layer and by more than 1 x 10^9 J m^{-2} below 1,200 m. It indicates that the water column was more favorably preconditioned in the Labrador Sea than in the SECF region during 2008 – 2014. Differently, B for W2017 shows slightly lower values from the surface to 1,300 m in the SECF region than in the Labrador Sea (see orange lines in Fig. 7). However, B in the Labrador Sea remains constant down to the depth of the deep halocline between LSW and North Atlantic Deep Water (NADW) at 1,700 m. In the SECF region, the deep halocline remained at ~1,300 m between 2016 and 2018 (see B$_s$ lines in Fig. 7a). Differently, in the Labrador Sea, the deep halocline deepened from 1,200 m for the mean to 1,735 m, 1,775 m and 1905 m in W2016, W2017 and W2018, respectively (see dashed lines in Fig. 7b). The deep halocline acts as a physical barrier for deep convection in both the SECF region and the Labrador Sea, but because the deep halocline is deeper in the Labrador Sea than in SECF region, the preconditioning is more favorable to a deeper convection in the Labrador Sea than in the SECF region. Summarizing, in winters 2016 - 2018 in the Labrador Sea, both atmospheric forcing and preconditioning of the water column granted the deepest convection depth in the Labrador Sea since the beginning of the Argo period (comparison of our results with those of Yashayaev and Loader, 2017). Contrasting, in SECF region, during the same period, the atmospheric forcing was close to climatological values, and the favorable preconditioning of the water column allowed 1,300 m depth convection, what was exceptional for the SECF region.

The Labrador Sea, SECF region and Irminger Sea are three distinct deep convection sites (e.g. Yashayaev et al., 2007; Bacon et al., 2003; Pickart et al., 2003; Piron et al., 2017). In this work, we give new insights on the connections between the different sites, showing how lateral advection of fresh LSW formed in the Labrador Sea favored the preconditioning in the SECF region fostering deeper convection.

Climate models forecast increasing input of freshwater in the North Atlantic due to ice-melting under present climate change (Bamber et al., 2018), which could reduce, or even shut-down, the deep convection in the North Atlantic (Yang et al., 2016; Brodeau & Koenigk, 2016). We observed a fresh anomaly in the surface waters in regions close to the eastern coast of Greenland in 2016 that extended to the whole Irminger Sea in 2017 (Fig. S6). However, this surface freshening did not hamper the deep convection in the SECF region possibly because the surface water also cooled. Swingedouw et al., 2013 indicated that the freshwater signal due to Greenland ice sheet melting is mainly accumulating in the Labrador Sea. However, no negative anomaly of S was detected in the

14

surface waters of the Labrador Sea (Fig. S6). It might be explained by the intense deep convection affecting the Labrador Sea since 2014 that could have transferred the surface freshwater anomaly to the ocean interior. This suggests that, in the last years, the interactions between expected climate change anomalies and the natural dynamics of the system combined to favor very deep convection. This however does not foretell the long term response to climate change.

6. CONCLUSIONS

During 2015 – 2018 winter deep convection happened in the SECF region reaching deeper than 1,300 m. The deep convection of W2015 was observed over a larger region and during a longer period of time than the deep convection events of winters 2016, 2017 and 2018. Despite these differences, it is the first time that deep convection, with maximum convection depth larger than 1,300 m, was observed in this region during four consecutive winters.

The atmospheric forcing and preconditioning of the water column was evaluated in terms of buoyancy. We showed that the atmospheric forcing is 10% weaker when evaluated in terms of buoyancy than in terms of heat because of the non-negligible effect of the freshwater flux. The analysis of the preconditioning of the water column in terms of buoyancy to be removed (B) and its thermal and salinity terms (B_θ and B_s) revealed that B_θ dominated the B profile from the surface to 800 m and B_s reduced the B in the 800 – 1,000 m layer because of low salinity of LSW. Deeper, B_s increased B due to the deep halocline (LSW-ISOW) that acted as a physical barrier limiting the depth of the convection.

During 2016 – 2018, the air-sea buoyancy losses were close to the climatological values and the very deep convection was possible thanks to the favorable preconditioning of the water column. It was surprising that these events reached convection depths similar to those observed in W2012 and W2015, when the latter were provoked by high air-sea buoyancy loss intensified by the effect of strong wind stress. It was also surprising that the water column remained favorably preconditioned during three consecutive winters without strong atmospheric forcing. In this paper, we studied the reasons why this happened.

The preconditioning for deep convection during 2016 – 2018 was particularly favorable due to the combination of two types of hydrographic anomalies affecting different depth ranges. First, the surface and intermediate waters (down to 800 m) were favorably preconditioned because buoyancy (density) decreased (increased) due to the cooling caused by the atmospheric forcing. Second,

15

480   buoyancy (density) increased (decreased) in the layer 1,200 – 1,400 m due to the decrease in S

481   caused by the lateral advection of fresher LSW formed in the Labrador Sea. The S anomaly of this

482   layer resulted in a deeper deep halocline. Hence, the cooling of the intermediate water was essential

483   to reach convection depth of 800 – 1,000 m, and the freshening in the layer 1,200 – 1,400 m and the

484   associated deepening of the deep halocline, allowed the very deep convection (> 1,300 m) in W2016

485   – W2018.

486   **Author contribution**: PZ treated and analyzed the data. PZ and HM interpreted the results. PZ, HM

487   and VT discussed the results and wrote the paper.

499

500   **REFERENCES**

501   Argo Data Management Team: Argo user's manual V3.2. https://doi.org/10.13155/29825, 2017

502   Argo group: Argo float data and metadata from Global Data Assembly Centre (Argo GDAC),

503   SEANOE, https://doi.org/10.17882/42182 ,2019

504   Bacon, S.: Circulation and Fluxes in the North Atlantic between Greenland and Ireland. *Journal of*

505   *Physical Oceanography*, *27*(7), 1420–1435. *https://doi.org/10.1175/1520-*

506   *0485(1997)027<1420:CAFITN>2.0.CO;2*, 1997.

507   Bacon, S., Gould, W. J. and Jia, Y.: Open-ocean convection in the Irminger Sea, Geophys. Res. Lett.,

508   30(5), 1246, doi:10.1029/2002GL016271, 2003.

509   Bamber, J. L., Tedstone, A. J., King, M. D., Howat, I. M., Enderlin, E. M., van den Broeke, M. R., & Noel,

16

B.: Land Ice Freshwater Budget of the Arctic and North Atlantic Oceans: 1. Data, Methods, and Results, *Journal of Geophysical Research: Oceans*, 1–11, https://doi.org/10.1002/2017JC013605, 2018.

Billheimer, S., & Talley, L. D.: Near cessation of Eighteen Degree Water renewal in the western North Atlantic in the warm winter of 2011 – 2012, *118*(November), 6838–6853, https://doi.org/10.1002/2013JC009024, 2013.

Brodeau, L., & Koenigk, T.: Extinction of the northern oceanic deep convection in an ensemble of climate model simulations of the 20th and 21st centuries, *Climate Dynamics*, *46*(9–10), 2863–2882. https://doi.org/10.1007/s00382-015-2736-5, 2016.

Centurioni and Gould, W. J.: Winter conditions in the Irminger Sea observed with profiling floats, *Journal of Marine Research*, 62, 313–336, 2004.

Daniault, N., Mercier, H., Lherminier, P., Sarafanov, A., Falina, A., Zunino, P., Gladyshev, S. : The northern North Atlantic Ocean mean circulation in the early 21st century, *Progress in Oceanography*, *146*(June), 142–158, https://doi.org/10.1016/j.pocean.2016.06.007, 2016.

de Boyer Montégut, C., Madec, G., Fischer, A. S., Lazar, A., & Iudicone, D.: Mixed layer depth over the global ocean: An examination of profile data and a profile-based climatology, *Journal of Geophysical Research C: Oceans*, *109*(12), 1–20, https://doi.org/10.1029/2004JC002378, 2004.

de Jong, M.F., Oltmanns, M., Karstensen, J., and de Steur, L.: Deep Convection in the Irminger Sea Observed with a Dense Mooring Array, *31*(February), 50–59, https://doi.org/10.5670/oceanog.2018.109, 2018.

de Jong, M. F., & de Steur, L.: Strong winter cooling over the Irminger Sea in winter 2014–2015, exceptional deep convection, and the emergence of anomalously low SST, *Geophysical Research Letters*, *43*(13), 7106–7113. https://doi.org/10.1002/2016GL069596, 2016.

de Jong, M. F., Van Aken, H. M., Våge, K., & Pickart, R. S.: Convective mixing in the central Irminger Sea: 2002-2010, *Deep-Sea Research Part I: Oceanographic Research Papers*, *63*, 36–51. https://doi.org/10.1016/j.dsr.2012.01.003, 2012.

Dee, D. P., Uppala, S. M., Simmons, A. J., Berrisford, P., Poli, P., Kobayashi, S., Vitart, F.: The ERA-Interim reanalysis: Configuration and performance of the data assimilation system, *Quarterly Journal of the Royal Meteorological Society*, *137*(656), 553–597. https://doi.org/10.1002/qj.828, 2011.

17

540 Fröb, F., Olsen, A., Våge, K., Moore, G.W.K., Yashayaev, I., Jeansson, E. & Rajasakaren B.: Irminger Sea
541   deep convection injects oxygen and anthropogenic carbon to the ocean interior. NATURE
542   COMMUNICATIONS | 7:13244 |
543   DOI:10.1038/ncomms13244|www.nature.com/naturecommunications, 2016.

544 Gaillard, F., Reynaud, T., Thierry, V., Kolodziejczyk, N., & Von Schuckmann, K.: In situ-based reanalysis
545   of the global ocean temperature and salinity with ISAS: Variability of the heat content and steric
546   height. *Journal of Climate*, *29*(4), 1305–1323. https://doi.org/10.1175/JCLI-D-15-0028.1, 2016.

547 Gill, A. E. (1982), Atmosphere-Ocean Dynamics, vol. 30, Academic, San Diego, CA.
548
549 Good, S. A., Martin, M. J., & Rayner, N. A.: EN4: Quality controlled ocean temperature and salinity
550   profiles and monthly objective analyses with uncertainty estimates. *Journal of Geophysical
551   Research: Oceans*, *118*(12), 6704–6716. https://doi.org/10.1002/2013JC009067, 2013.

552 Josey, S. A., Hirschi, J. J.-M., Sinha, B., Duchez, A., Grist, J. P., Marsh, R.: The Recent Atlantic Cold
553   Anomaly: Causes, Consequences, and Related Phenomena. Annual Review of Marine Science,
554   10 (1). 475-501.https://doi.org/10.1146/annurev-marine-121916-063102, 2018

555 Kieke, D., & Yashayaev, I.: Studies of Labrador Sea Water formation and variability in the subpolar
556   North Atlantic in the light of international partnership and collaboration. *Progress in
557   Oceanography*, *132*, 220–232. https://doi.org/10.1016/j.pocean.2014.12.010, 2015a.

558 Kieke, D., & Yashayaev, I.: Studies of Labrador Sea Water formation and variability in the subpolar
559   North Atlantic in the light of international partnership and collaboration, *Progress in
560   Oceanography*, *132*, 220–232, https://doi.org/10.1016/j.pocean.2014.12.010, 2015b.

561 Kolodziejczyk, N., Prigent-Mazella A., and Gaillard F. (2017). ISAS-15 temperature and salinity gridded
562   fields. **SEANOE**. http://doi.org/10.17882/52367

563 Lavender, K. L.,Davis, R. E., & Owens, W. B.: Mid-depth recirculation observed in the interior
564   Labrador and Irminger seas by direct velocity measurements. NATURE |VOL 407 | 7
565   SEPTEMBER 2000 |www.nature.com, 2000.

566 Marshall, J., & Schott, F.: Open-Ocean Convection ' Theory , and Models Observations ,. *Reviews of
567   Geophysics*, *37*(98), 1–64. https://doi.org/10.1029/98RG02739, 1999.

568 Ollitrault, M., & Colin de Verdière, A.: The Ocean General Circulation near 1000-m Depth, *Journal of
569   Physical Oceanography*, *44*(1), 384–409. https://doi.org/10.1175/JPO-D-13-030.1, 2014.

570 Pickart, R. S., Torres, D. J. and Clarke, R. A.: Hydrography of the Labrador Sea during active

18

571   convection, J. Phys. Oceanogr., 32, 428–457, 2002.

572 Pickart, R. S., Straneo, F., & Moore, G. W. K.: Is Labrador Sea Water formed in the Irminger basin?
573   *Deep-Sea Research Part I: Oceanographic Research Papers*, *50*(1), 23–52,
574   https://doi.org/10.1016/S0967-0637(02)00134-6, 2003.

575 Piron, A., Thierry, V., Mercier, H., & Caniaux, G.: Argo float observations of basin-scale deep
576   convection in the Irminger sea during winter 2011–2012. *Deep-Sea Research Part I:*
577   *Oceanographic Research Papers*, *109*, 76–90. https://doi.org/10.1016/j.dsr.2015.12.012, 2016.

578 Piron, A., Thierry, V., Mercier, H., & Caniaux, G.: Gyre-scale deep convection in the subpolar North
579   Atlantic Ocean during winter 2014–2015. *Geophysical Research Letters*, *44*(3), 1439–1447.
580   https://doi.org/10.1002/2016GL071895, 2017.

581 Rhein, M, Steinfeldt, R, Kieke, D, Stendardo, I and Yashayaev, I.: Ventilation variability of Labrador
582   Sea Water and its impact on oxygen and anthropogenic carbon: a review, *Philosophical*
583   *Transactions of the Royal Society A: Mathematical, Physical and Engineering Sciences*,
584   375(2102). 20160321. doi:10.1098/rsta.2016.0321, 2017.

585 Schmidt, S., & Send, U.: Origin and Composition of Seasonal Labrador Sea Freshwater, *Journal of*
586   *Physical Oceanography*, *37*(6), 1445–1454. https://doi.org/10.1175/JPO3065.1, 2007.

587 Straneo, F, Pickart, R.S., Lavender, K.: Spreading of Labrador sea water: an advective-diffusive study
588   based on Lagrangian data. Deep-Sea Research Part I-Oceanographic Research Papers. 50:701-
589   719, 2003.

590 Swingedouw, D., Rodehacke, C. B., Behrens, E., Menary, M., Olsen, S. M., & Gao, Y.: Decadal
591   fingerprints of freshwater discharge around Greenland in a multi-model ensemble, 695–720.
592   https://doi.org/10.1007/s00382-012-1479-9, 2013.

593 Yang, Q., Dixon, T. H., Myers, P. G., Bonin, J., Chambers, D., & Van Den Broeke, M. R.: Recent
594   increases in Arctic freshwater flux affects Labrador Sea convection and Atlantic overturning
595   circulation, *Nature Communications*, *7*, 1–7. https://doi.org/10.1038/ncomms10525, 2016.

596 Yashayaev, I., Bersch, M., & van Aken, H. M.: Spreading of the Labrador Sea Water to the Irminger
597   and Iceland basins, *Geophysical Research Letters*, *34*(10), 1–8.
598   https://doi.org/10.1029/2006GL028999, 2007.

599 Yashayaev, I., & Clarke, A.: Evolution of North Atlantic Water Masses Inferred From Labrador Sea
600   Salinity Series, *Oceanography*, *21*(1), 30–45. https://doi.org/10.5670/oceanog.2008.65, 2008.

601 Yashayaev, I., & Loder, J. W.: Recurrent replenishment of Labrador Sea Water and associtated

602 decadal-scale variability, *Journal Geophysical Research: Oceans*, *121*, 8095–8114,

603 https://doi.org/10.1002/2016JC012046, 2016.

604 Yashayaev, I., & Loder, J. W.: Further intensification of deep convection in the Labrador Sea in 2016.

605 *Geophysical Research Letters*, *44*(3), 1429–1438. https://doi.org/10.1002/2016GL071668, 2017.

606

607

608

609

610

611

612

613

614

615

616

617

618

619

620

621

622

623

624

20

625 Table 1. Properties of the deep convection SECF and in the Labrador Sea in winters 2015 – 2018. We
626 show: the maximal MLD observed, the aggregate maximum depth of convection, the σ_0, S and θ of
627 the winter mixed layer formed during the convection event and n, which is the number of Argo
628 profiles indicating deep convection. The uncertainties given with σ_0, S and θ are the standard
629 deviation of the n values considered to estimate the mean values.

SECF	Maximal MLD (m)	Aggregate max. depth of convection (m)	σ_0	Salinity	θ	n
W2015			27.733 ±	34.866±	3.478 ±	
	1710	1205	0.007	0.013	0.130	29
W2016			27.746±	34.871±	3.388 ±	
	1575	1471	0.002	0.003	0.032	3
W2017			27.745±	34.868±	3.364±	
	1400	1251	0.007	0.007	0.109	3
W2018			27.748±	34.859±	3.263±	
	1300	1300	0.001	0.003	0.031	2
LABRADOR SEA	Maximal MLD	Aggregate max. depth of convection (m)	σ_0	Salinity	θ	n
W2015	1675	1504	27.733 ± 0.009	34.842 ± 0.010	3.279 ± 0.036	41
W2016	1801	1620	27.743 ± 0.006	34.836 ± 0.010	3.124 ± 0.047	18
W2017	1780	1674	27.752 ± 0.008	34.853 ± 0.009	3.172 ± 0.029	26
W2018	2020	1866	27.756 ± 0.006	34.855 ± 0.010	3.145 ± 0.083	13

630

631

632

633 **FIGURES**

21
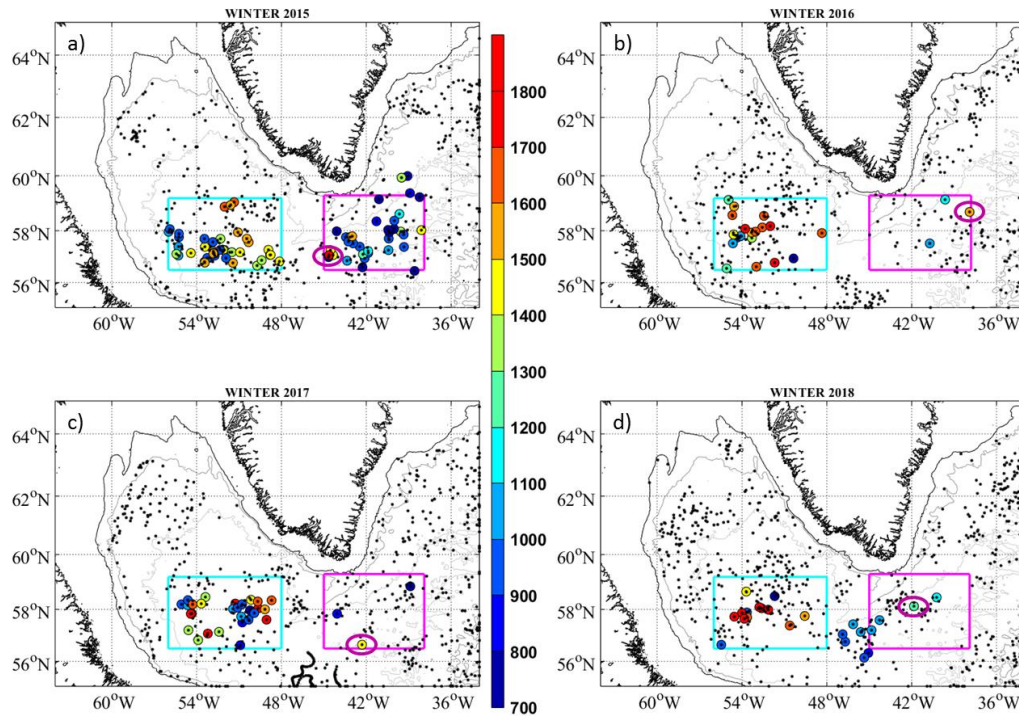
Figure 1. Positions of all Argo float north of 55°N in the Atlantic between 1 January and 30 April a) 2015, b) 2016, c) 2017 and d) 2018 (black and colored points). The colored points and color bar indicate the mixed layer depth (MLD) when MLD was deeper than 700 m. The pink circles indicate the position of the maximal MLD observed SECF each winter. The pink and cyan boxes delimit the regions used for estimating the time series of atmospheric forcing and the vertical profiles of buoyancy to be removed in the SECF region and the Labrador Sea, respectively (SECF: 56.5°N – 59.3°N and 45.0°W – 38.0°W, Labrador Sea: 56.5°N – 59.2°N and 56°W – 48°W).

642
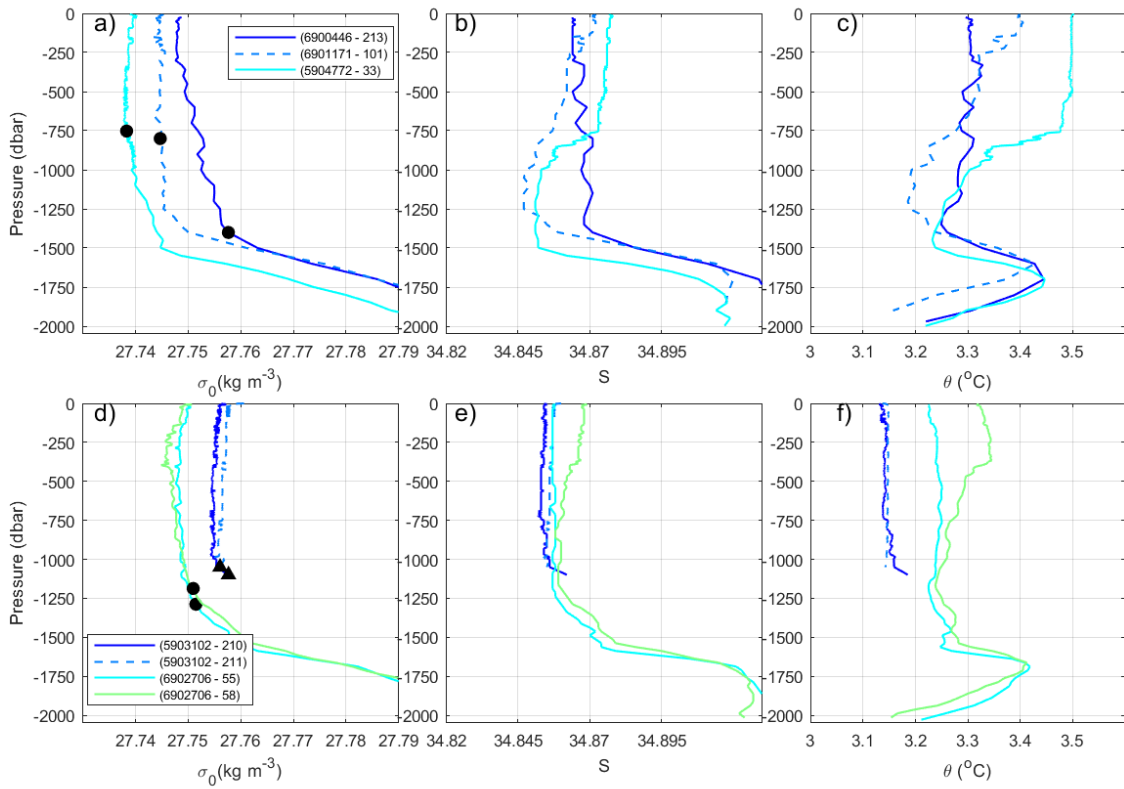
Figure 2. Vertical distribution of σ_0, S and θ of Argo profiles showing MLD deeper than 700 m SECF in Winter 2017 (a, b and c) and in Winter 2018 (d, e, f). The black points indicate the MLD. The triangles in d) are the MLD which coincided with the maximal profiling pressure reached by the float. In the legend, the float and cycle of each profile are indicated.

647
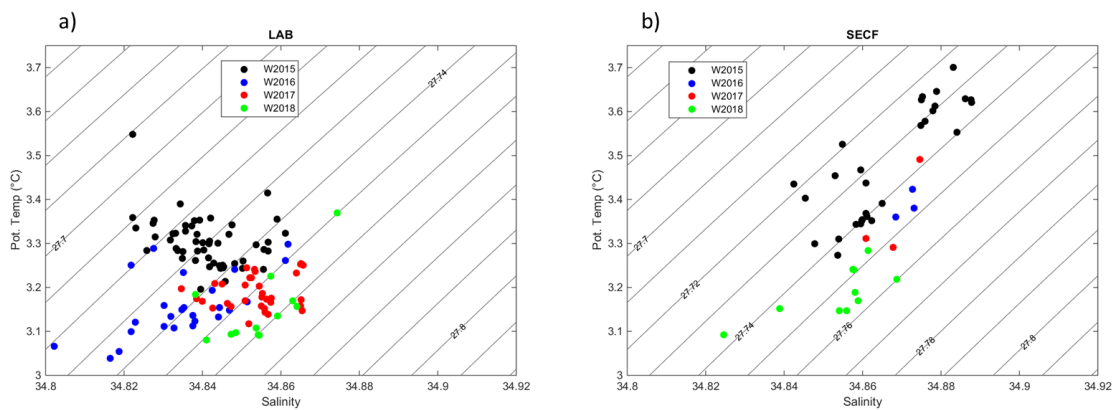
Figure 3. TS diagrams in the mixed layer for profiles with MLD deeper than 700 m during winters 2015, 2016, 2017 and 2018 for a) the Labrador Sea and b) SECF. The properties of the mixed layers were estimated as the vertical means between 200 m and the MLD.

23

SE CAPE FAREWELL
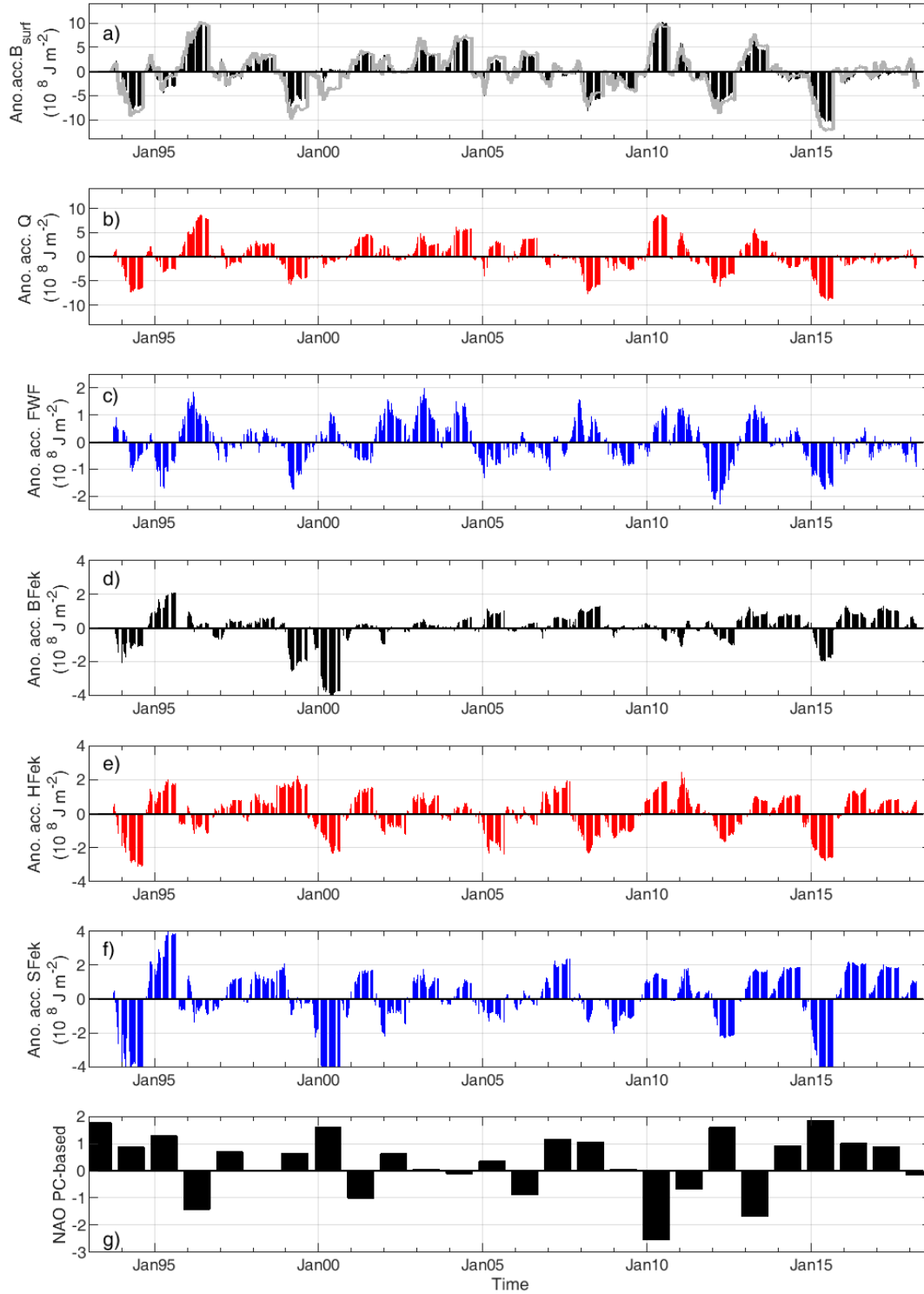
651
652   **Figure 4.** Time series of anomalies of accumulated a) Bsurf*, b) Q, c) FWF* d) BF$_{ek}$,e) HF$_{ek}$ and f) SF$_{ek}$,

averaged in the SECF region. They are anomalies with respect to 1993 – 2016. The accumulation was from 1 September to 31 August the following year. The winter NAO index (Hurrel et al., 2018) is also represented in g). Gray line in a) is the sum of the anomalies of accumulated B_{surf}* and BF_{ek}. Note that the range of values in the y-axis is not the same in all the plots.
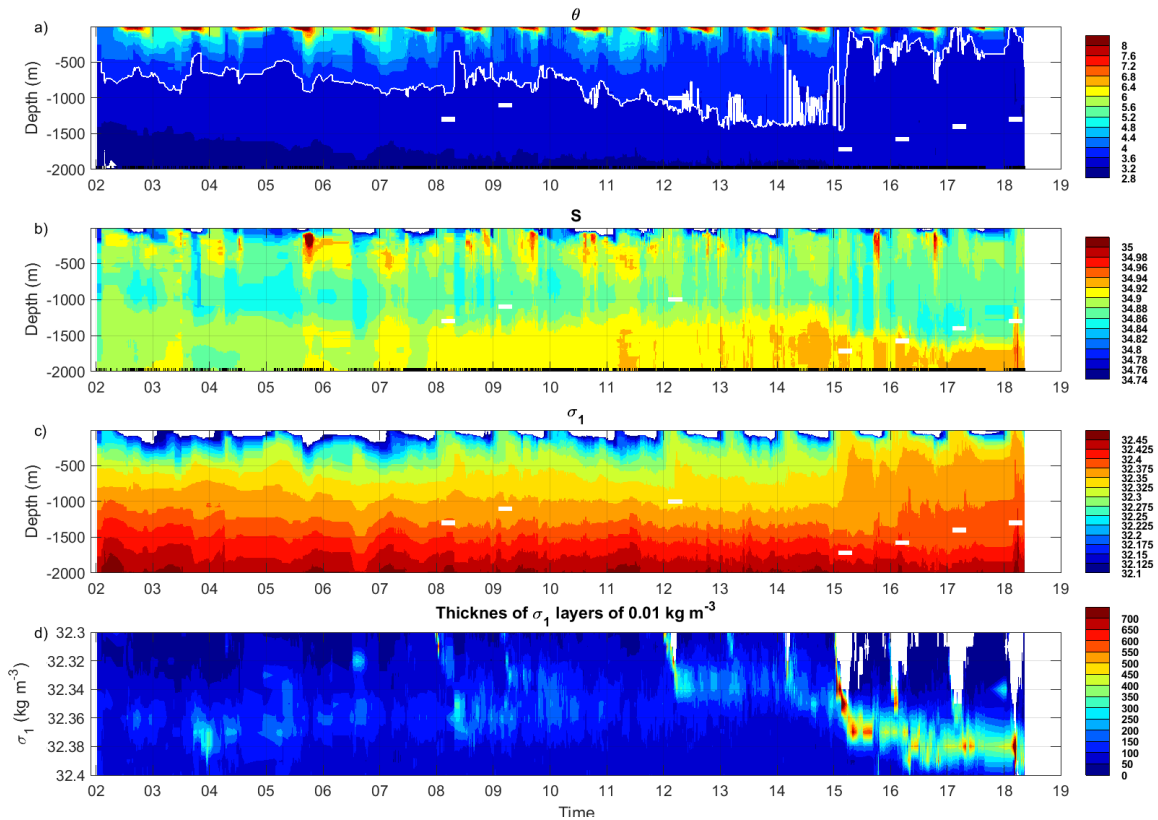

Figure 5. Time-evolutions of vertical profiles measured from Argo floats in the SECF region: a) θ ; b) S; c) σ_1 and d) thickness of 0.01 kg m^{-3} thick σ_1 layers. The white horizontal bars in plots a), b) and c) indicate the maximal convection depth observed in Irminger Sea or SECF when deep convection occurred. The white line in plot a) indicates the depth of the isotherm 3.6 °C. The black vertical ticks on the x-axes of plot b) indicate times of Argo measurements. These figures were created from all Argo profiles reaching deeper than 1000 m in the SECF region (56.5° – 59.3°N, 45°– 38°W, pink box in Fig. 1). The yearly numbers of Argo profiles used in this figure are shown in Fig. S5.

667
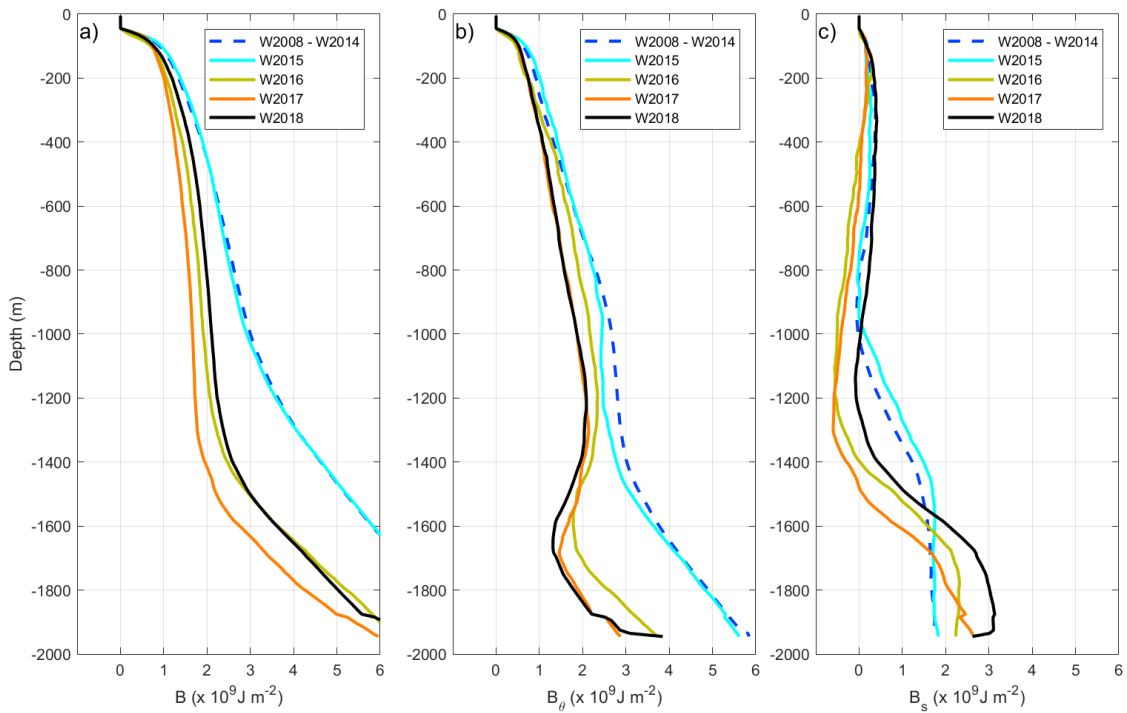
Figure 6. Vertical profile of a) the buoyancy to be removed (B), b) the thermal component (B_θ) and c) the salinity component (B_s). They were calculated from all Argo data measured in the SECF box (see Fig. 1) in September before the winter indicated in the legend. For W2015 and W2018, we considered data from 15/08/2017 to 30/09/2017 because not enough data were available in September. The number of Argo profiles taken into account to estimate the B profiles was more than ten for all the winters.

674
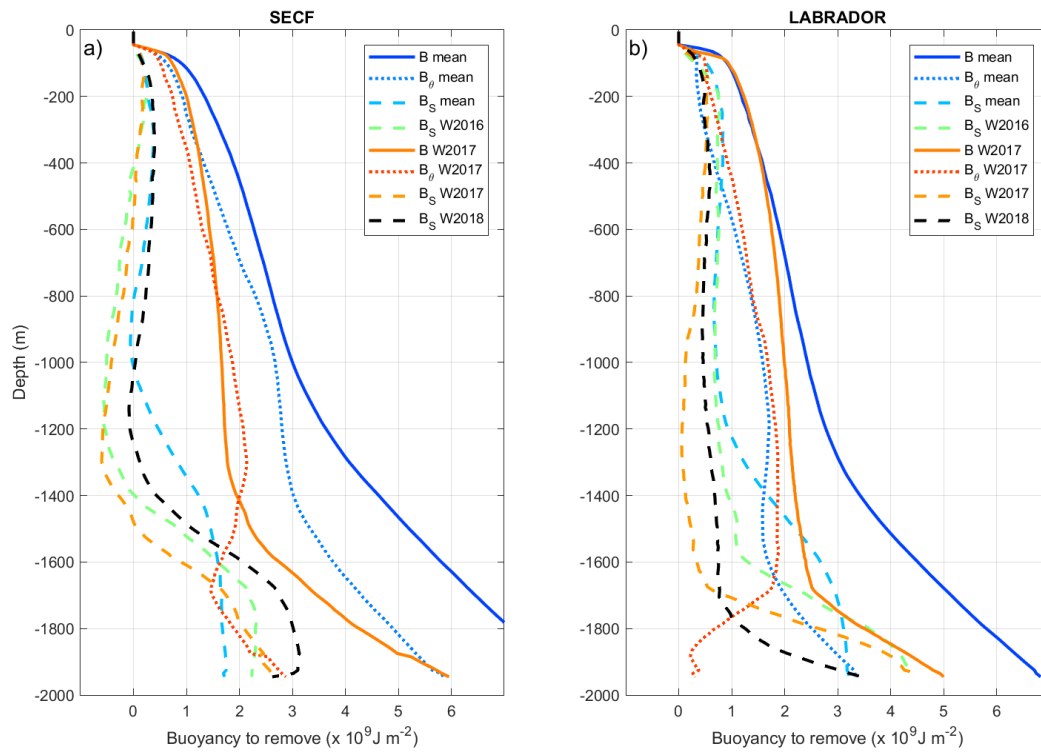
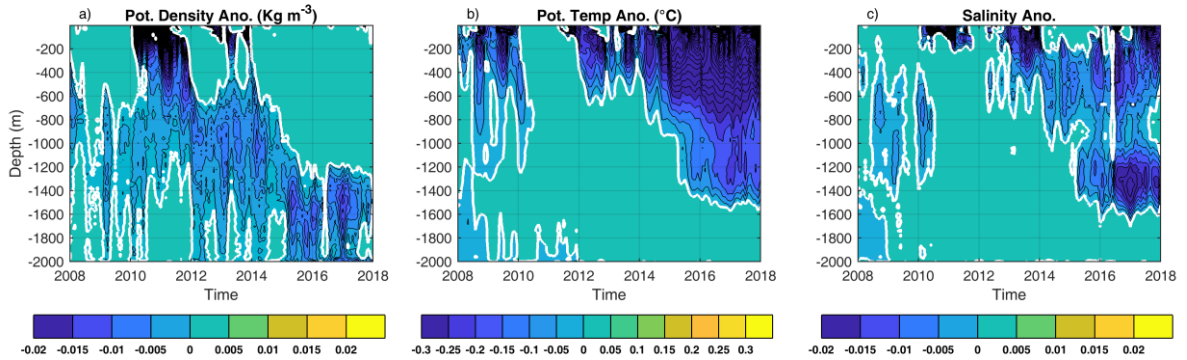**Figure 7.** Decomposition of profiles of buoyancy to be removed (B, continuous lines) in its thermal (B_θ, dotted lines) and salinity (B_s, dashed lines) components in a) the SECF region; b) the Labrador Sea. The B_s components for W2016 and W2018 were added to show the evolution of the depth of the deep halocline.

679

680

681
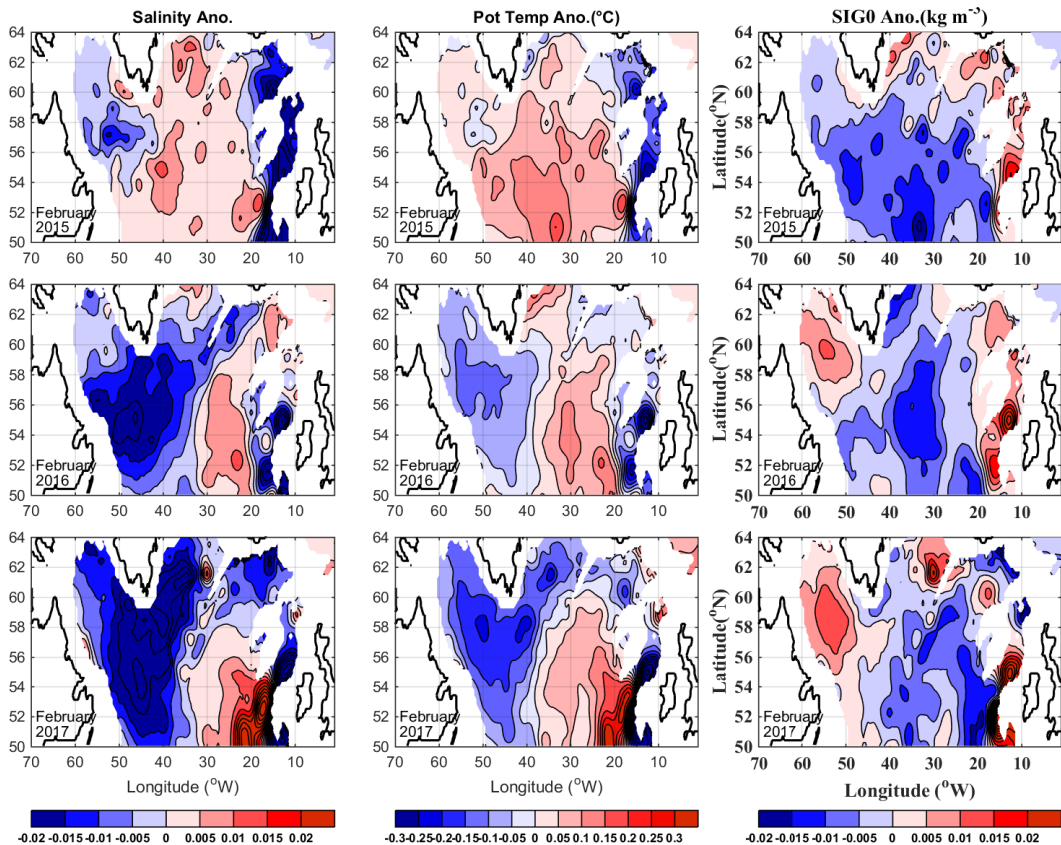
27

682

Figure 8. Evolution of vertical profiles of monthly anomalies of a) σ_0, b) θ and c) S, at 58°N, 40°W. The anomalies were estimated from the ISAS database (Gaillard et al., 2016), and were referenced to the monthly mean estimated for 2002 – 2016.

686
687 **Figure 9.** Horizontal distribution of the anomalies of S (left panels), θ (central panels) and σ_0 (right panels) in the layer 1,200 – 1,400 m in February 2015 (upper panels), February 2016 (central panels) and February 2017 (lower panels). The monthly anomalies were estimated from ISAS database and were referenced to the period 2002 – 2016.

28